energies

MDPI

Article

Dynamic Stall of a Vertical-Axis Wind Turbine and Its Control Using Plasma Actuation

Lu Ma, Xiaodong Wang *, Jian Zhu and Shun Kang

Key Laboratory of Power Station Energy Transfer Conversion and System, Ministry of Education, North China Electric Power University, Beijing 102206, China; 1162102037@ncepu.edu.cn (L.M.); 1111170919@ncepu.edu.cn (J.Z.); Kangs@ncepu.edu.cn (S.K.)

* Correspondence: Wangxd@ncepu.edu.cn

Received: 27 August 2019; Accepted: 26 September 2019; Published: 30 September 2019

Abstract: In this paper, a dynamic stall control scheme for vertical-axis wind turbine (VAWT) based on pulsed dielectric-barrier-discharge (DBD) plasma actuation is proposed using computational fluid dynamics (CFD). The trend of the wind turbine power coefficient with the tip speed ratio is verified, and the numerical simulation can describe the typical dynamic stall process of the H-type VAWT. The tangential force coefficient and vorticity contours of the blade are compared, and the regular pattern of the VAWT dynamic stall under different tip speed ratios is obtained. Based on the understanding the dynamic stall phenomenon in flow field, the effect of the azimuth of the plasma actuation on the VAWT power is studied. The results show that the azimuth interval of the dynamic stall is approximately 60° or 80° by the different tip speed ratio. The pulsed plasma actuation can suppress dynamic stall. The actuation is optimally applied for the azimuthal position of 60° to 120°.

Keywords: DBD plasma actuation; dynamic stall; vertical-axis wind turbine; active flow control

1. Introduction

Dielectric-barrier-discharge (DBD) plasma actuation is an active flow control technology developed in the mid-1960s [1]. The actuator is a plasma-generating device, which is composed of two electrodes, dielectric between the electrodes, and an external high voltage power source. When the actuator is working, the air near the electrode is ionized to ions and electrons. Due to the asymmetry of the electrode arrangement, the ions move in an orientated direction within the electric field, generating a body force that drives the neutral gas molecules to produce a tangential jet, achieving boundary layer flow control. DBD plasma actuation has good performance in boundary layer flow separation control [2], dynamic stall vortex control [3], and so on [4].

The dynamic stall phenomenon can be removed by unsteady pitch control of the blade and the boundary layer separation [5]. Dynamic stall is an inherent feature of VAWT. The angle of attack and relative speed of a blade are changing dramatically during each VAWT rotation cycle. The boundary layer separates and a leading edge vortex is formed on the suction side. This causes the VAWT dynamic stall. Dynamic stall will bring about VAWT structure vibration, noise, and efficiency reduction [6]. VAWT dynamic stall is a complex unsteady flow phenomenon. When the blade moves, the relative velocity and direction are time varying, and the blade is affected by the upstream wake. Although researchers are extremely interested in using flow control methods to improve wind turbine performance [7–10], few researchers have addressed the problem of VAWT dynamic stall. Previous works have only focused on the relationship between the lift/drag and the angle of attack [11], or simply flow field [12,13]. However, there is still a need for investigating the correspondence between the vortex motion and the tangential force of a blade.

There is a considerable amount of research on plasma dynamic stall control for an oscillating airfoil or a flat plate. There is still little knowledge about plasma control of VAWT. In 2006, Post & Corke [3] placed the actuator at the leading edge of NACA0015 airfoil, and the effect of DBD plasma for flow separation and dynamic stall control on an oscillating airfoil was studied experimentally. It was found that the plasma actuation was able to suppress separation and delay stall, and the pulsed actuation was more advantageous. Sato et al. [14] studied the lift enhancement of an oscillating plate by plasma actuation through wind tunnel experiments and numerical simulations. They pointed out that plasma actuation could effectively suppress the flow separation on the flat plate during the up-stroke motion. Phan & Shin [15] using numerical method investigated the impact on the aerodynamic performance at different plasma actuation parameters and actuation positions for an oscillating NACA0012 airfoil. They believed that plasma could increase the lift of the airfoil and suggested to consider the energy consumption of the actuator to achieve the optimal control authority. Greenblatt et al. [16,17] placed a plasma actuator on the leading edge of a small vertical-axis wind turbine and conducted related research. The actuator is placed at the leading edge in a pulsed actuation mode. The results showed that after applying control, the power of the wind turbine increased and the fluctuation decreased, because plasma actuation reduced the leading edge vortex. They also argued that plasma actuation is only effective on the upwind side; however, it was not clear what specific azimuthal interval should be applied actuation. It is valuable and practical to formulate a scientific and economic control strategy to reduce the excited energy consumption and increase the power of the wind turbine.

Two methods can be used to study dynamic stall phenomena: numerical methods [18,19] and wind tunnel experimental methods [20]. Due to the complexity of the VAWT dynamic stall phenomenon, wind tunnel experiments are difficult to capture the full detailed flow field. Therefore, the numerical simulation method is used to study the VAWT dynamic stall problem. The load of VAWT can be calculated using the empirical formula model [21] and the theoretical model [22]. The former is calculated formula fitted by the experimental data, which is easy to implement and low in cost; the latter is mainly solved by the CFD method, and a complex flow field with high kinetic energy and shearing can be obtained, but its more time consuming. Buchner et al. [23] used a theoretical model to study the dynamic stall phenomenon of VAWT and found that the tip speed ratio was less than 3, which significantly reduced the power of VAWT. Most of the dynamic stall effects occur in the low tip speed ratio (less than 3), while the VAWTs actually operate mainly within it, which highlights the industrial relevance of the dynamic stall problem.

A suitable actuator simplified model needs to be selected for numerical simulation of DBD plasma flow control. Shyy et al. [24], Massines et al. [25], Suzen et al. [26], and Abdollahzadeh et al. [27–29] proposed their actuator simplified models based on different assumptions, respectively. The most widely used is the phenomenological model proposed by Shyy et al., which loads the plasma reduced body force into the fluid momentum equation as a source term. The advantages of the Shyy's model are simplicity, fast response, ease of application, and so on. However, the oversimplified model severely overestimates the body forces generated by the plasma actuator. Therefore, the experimental correction of the Shyy's model must be performed before the numerical calculation. The following literature use the corrected Shyy's model for numerical simulation studies [30,31]. Considering the complex unsteadiness of the VAWT dynamic stall and the accuracy of the phenomenological model, in this paper, the modified Shyy's model is selected for numerical simulation.

In this paper, the unsteady CFD method is used to study the dynamic stall phenomenon of VAWT at different tip speed ratios, and the azimuthal position corresponding to the start and end of dynamic stall is found. The modified plasma phenomenological model is used to analyze the influence of plasma actuation on VAWT in different azimuthal intervals. An optimal control strategy for dynamic stall of a vertical-axis wind turbine based on plasma actuation is proposed.

2. Computational Model and Numerical Method

2.1. H-Type VAWT Model

In this paper, a two-dimensional model is used for numerical simulation. The three-blade H-type VAWT model computational domain is shown in Figure 1, which is consistent with the reference [22,32]. D represents the diameter of the wind turbine. Inlet, outlet, upper, and lower boundary are 2.5D, 4.5D, and 2D from the VAWT center, respectively.

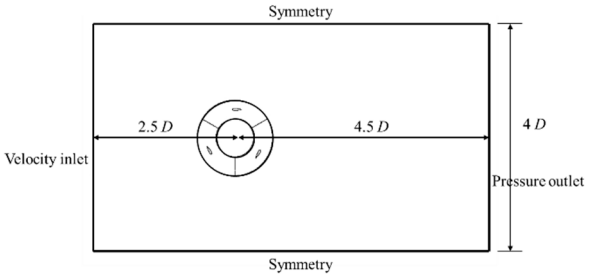

Figure 1. Computational domain and boundary conditions.

The radius of VAWT is R = 0.3 m. The blade adopts the NACA0022 airfoil with a chord length c = 0.1 m. The inlet velocity is U_∞ = 5.07 m/s. The rotational speed ω = 16.9~50.7 rad/s, are studied, corresponding to the tip speed ratio λ = 1 to 3. θ is the azimuth, and the position where the blade 1 is located in Figure 2 is defined as θ = 0°. θ = 0°~180° is the upwind side, and θ = 180°~360° is the downwind side.

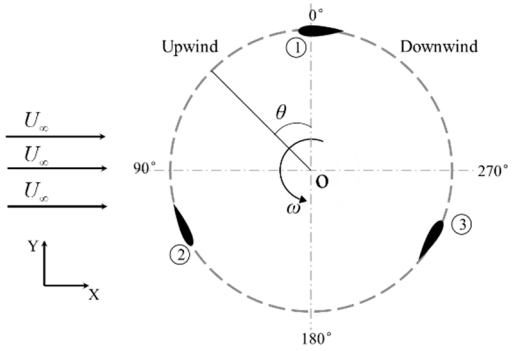

Figure 2. Position of each blade of VAWT.

The plasma actuator is placed at 5~90% c from the leading edge, and the purple triangle represents the plasma region (The actuator is placed at 30% c), as shown in Figure 3.

Figure 3. Position of the plasma actuator on a blade.

2.2. Plasma Actuator Model

The Shyy's model [24] simplifies the complex body force generated by plasma into linear electric field force. The basic mechanism of the actuator is shown in Figure 4.

Ignoring the secondary factors, assuming that the plasma density ρ_c is constant and the electric field is linearly distributed, the electric field distribution in the OAB is obtained as

$$\left|\vec{E}\right| = E_0 - k_1 x - k_2 y \tag{1}$$

where $E_0 = 1.2 \times 10^4$ kV/m is the maximum electric field strength, and the coefficients $k_1 = 1.8 \times 10^9$ kV/m^2 and $k_2 = 3.6 \times 10^9$ kV/m^2 are obtained from the electric field distribution [30].

The body force induced by the plasma actuator can be expressed as electric field force

$$\vec{F} = \vec{E}\rho_c e\alpha \tag{2}$$

where $e = 1.602 \times 10^{-19}$ C [24] is elementary charge, and $\rho_c = 1 \times 10^{17}$ m^3 [24]. The $\alpha = 0.3$ is the correction factor [30].

The duty cycle is: $D_{tc} = T_d/T$, where T_d is the duration of the plasma actuation and T is the period.

The original Shyy's model is a great oversimplification; hence, the model used in this paper is calibrated by experiment [33]. In the present study, the height and width of the plasma region in Figure 4 are OA = 2.5 mm and OB = 5 mm [34,35]. In Equation (2), The electric field strength is multiplied by the correction factor of 0.3. Figure 5 is the comparison between the computational and experimental [33] streamwise velocity distribution, where u_p is the plasma reduced velocity, and $u_{p,max} = 5.9$ m/s is the maximum plasma reduced velocity. The ordinate represents the distance from the wall. It can be seen from Figure 5 that the corrected model has a good agreement with the experimental values.

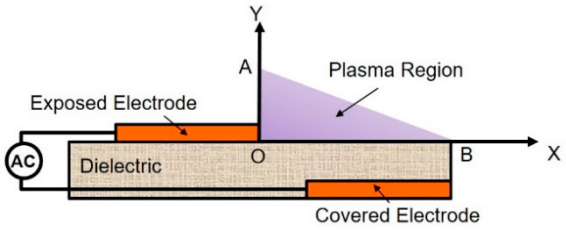

Figure 4. Sketch of the plasma actuator.

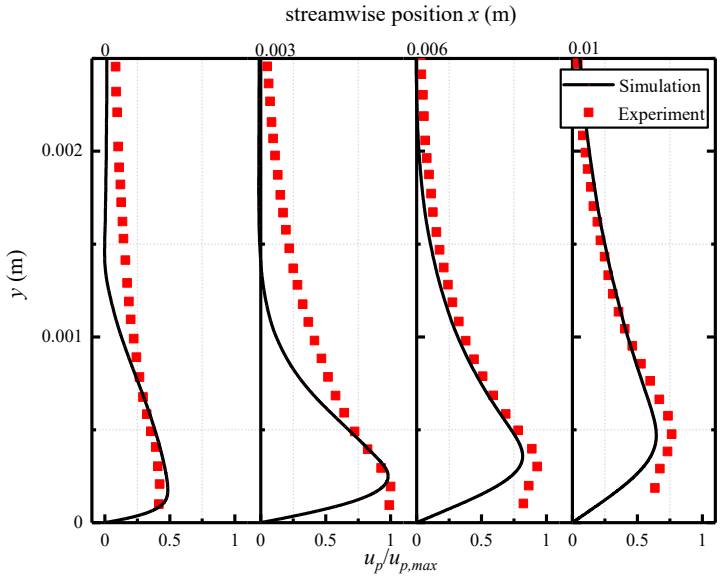

Figure 5. Velocity distribution at different streamwise positions.

2.3. Numerical Method and Boundary Conditions

Figure 6 shows the global mesh of the computational domain. The structured grid is generated, and the total number of cells is 300,000. The sliding mesh is used to establish the rotation domain and the number of cells is 260,000. The grids number along the circumference of a blade is 500. The first cell height of the blade is 0.01 mm, which guarantees $y^+ < 1$, as shown in Figure 7.

Inlet is velocity inlet. Outlet is pressure outlet. Upper and lower boundary are symmetry. The blade surface is a non-slip wall. The electric field force generated by the plasma actuation is loaded as a body force source term though the user-defined function.

Numerical simulations are calculated using ANSYS FLUENT. The turbulence model is *k*-ω SST model. The blades rotate 0.2 degrees per time step.

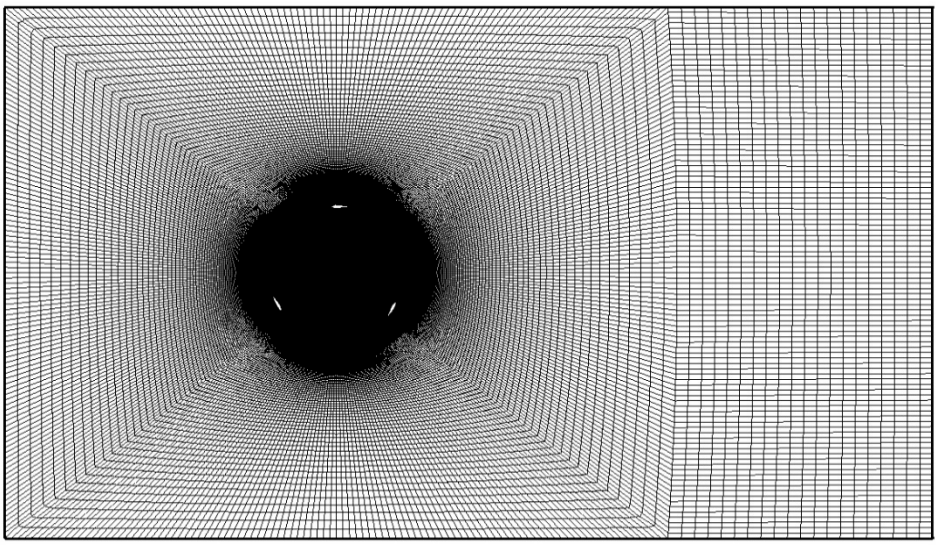

Figure 6. Global mesh of computational domain.

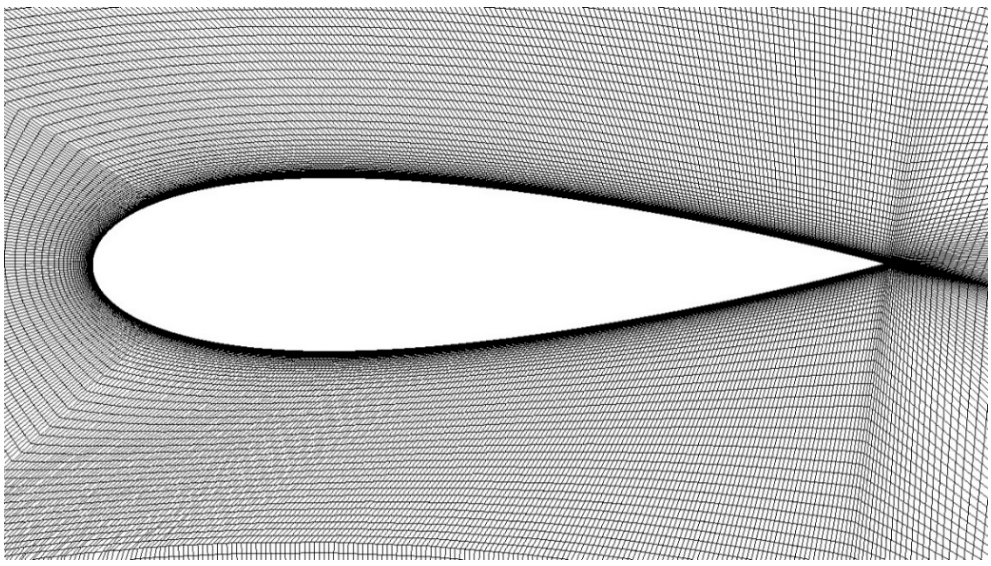

Figure 7. Mesh around the blade.

2.4. CFD Validation

In Figure 8a, grid sensitivity verification is performed on base-line case (U_∞ = 5.07 m/s, λ = 2.15) of three different numbers of cells. As a constant, the first cell height of the blade is 0.01 mm, which guarantees $y^+ < 1$. The grids number along the circumference of a blade are 500, 250, and 125,

respectively. As can be seen from the figure, the difference between the three grids is small. Considering the requirements of the plasma model for the grid, the fine mesh (260,000 cells) is selected.

VAWT dynamic stall is a complex unsteady flow phenomenon; hence, the time step sensitivity verification is necessary. Figure 8b shows the verification of three different the time step sizes on base-line case. It can be seen that large time step size (Δt = 0.0003 s) makes the tangential force larger. Since the frequency of the plasma pulsed actuation is high, the minimum time step size is selected. When the time step size is Δt = 0.0001 s, the blades rotate 0.2 degrees per time step.

It is important and necessary to choose a suitable turbulence model for numerical simulation. A large number of scholars [36–39] have used *k*-ω SST model to solve VAWT problems. Therefore, this paper does not perform additional verification on the turbulence model.

The convergence criterions are that all the parameters was set to 10^{-4} at each time step and the tangential force coefficient of a blade exhibits significant periodicity. Figure 9 shows the variation of the tangential force coefficient with azimuth over 15 cycles. As can be seen from the Figure 9, the solution of the last 10 cycles have converged. In this paper, we use the time average result of the last 10 cycles.

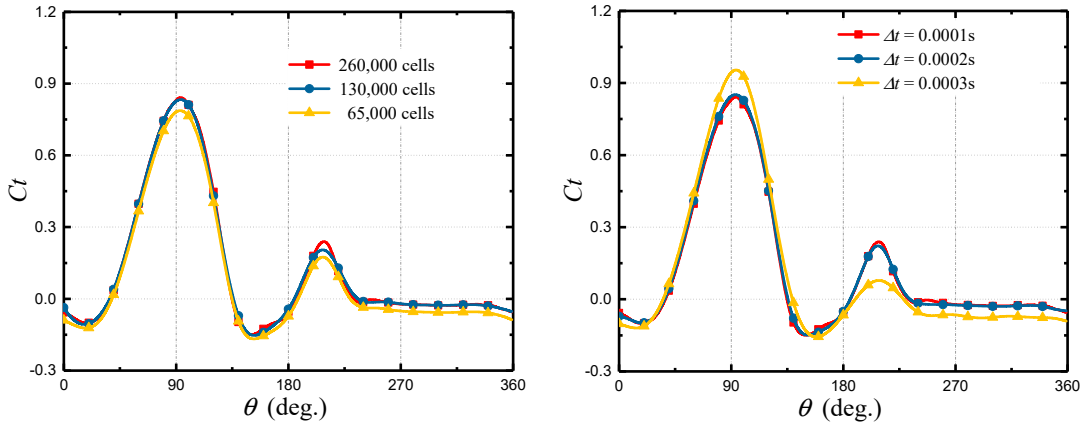

(**a**) Grid sensitivity (**b**) Time step sensitivity

Figure 8. CFD validation: the tangential force coefficient with azimuth.

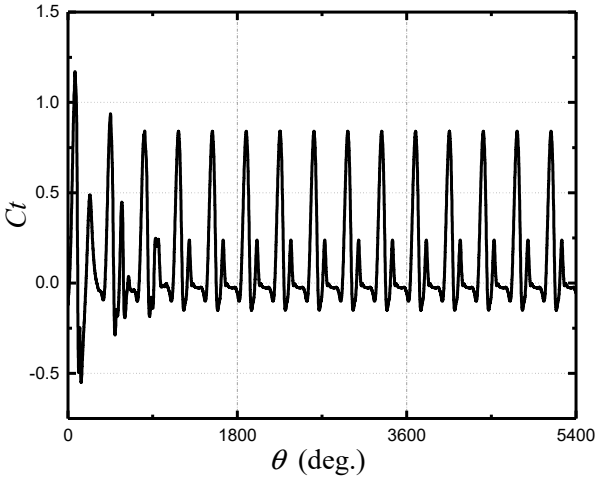

Figure 9. Convergence criterion: the tangential force coefficient with azimuth.

2.5. H-Type VAWT Aerodynamic Parameters

Several major aerodynamic parameters are described below to characterize VAWT dynamic stall.

The tip speed ratio λ is the blade linear velocity to the free stream velocity U_∞, which is used to describe the blades' rotation speed. It is defined as

$$\lambda = R\Omega / U_\infty \tag{3}$$

where R is the radius of the rotor and Ω is the angular velocity of the rotor.

The relative velocity ratio $\hat{U}_{rel}$ is the instantaneous relative velocity of the blade U_{rel} to the free stream velocity. It is defined as

$$\hat{U}_{rel} = \frac{U_{rel}}{U_\infty} \tag{4}$$

The angle of attack based on the instantaneous relative velocity is

$$\alpha_{rel} = \tan^{-1}\left(\frac{\sin\theta}{\lambda + \cos\theta}\right) \tag{5}$$

The α_{rel} varying with azimuth is shown in the Figure 10. It can be seen that the lower the tip speed ratio, the larger the amplitude of α_{rel}.

The tangential force coefficient C_t and the power coefficient C_p represent the ability of the blade and the rotor to generate energy, respectively.

The tangential force coefficient is defined as

$$C_t = \frac{F_t}{1/2\rho U_\infty^2 S} \tag{6}$$

where F_t is tangential force of a blade, and S is the maximum projected area of a blade.

The power coefficient is defined as

$$C_p = \frac{3F_t \cdot \lambda}{1/2\rho U_\infty^2 A} \tag{7}$$

where A is the frontal projected area of wind turbine.

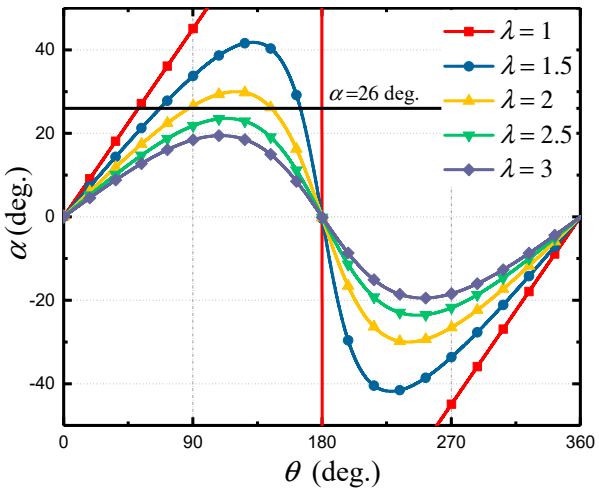

Figure 10. Angle of attack with azimuth.

2.6. Parameter Settings

The research scheme is shown in Table 1. In Scheme 1, the VAWT dynamic stall at five different tip speed ratios is studied. On the basis of Scheme 1, taking λ = 2.15 as an example, given the actuation duty cycle, and the pulse actuation frequency f, the effects of five plasma actuator positions on VAWT

are investigated. In Scheme 3, given the plasma actuator position, the effects of 10 plasma actuation intervals on VAWT dynamic stall are studied.

Table 1. Parameters of the simulations.

Parameter Settings	λ	Actuator Position	*Dtc*	*f*/Hz	Actuation Interval
Scheme 1	1~3	-	-	-	-
Scheme 2	2.15	5 different positions	0.2	383	-
Scheme 3	2.15	0.3*c*	0.2	383	10 different actuation intervals

3. Results and Discussion

3.1. Computational Results Verification

Figure 11 shows the comparison of the experimental data [32] and the two-dimensional numerical simulation data for wind turbine power coefficient. It can be found that the simulation results of both Zuo et al. [22] and this paper can reflect the variation tendency of C_p, but the numerical values are always larger than the experimental values. Because the two-dimensional numerical simulations ignore the end loss of the three-dimensional blades [40] and the influence of the support structure. Reference [40] pointed out that the two-dimensional URANS simulation can capture most of the details for the VAWT flow field. This paper mainly studies the flow separation and control technology on the VAWT, so the two-dimensional URANS simulation is adopted.

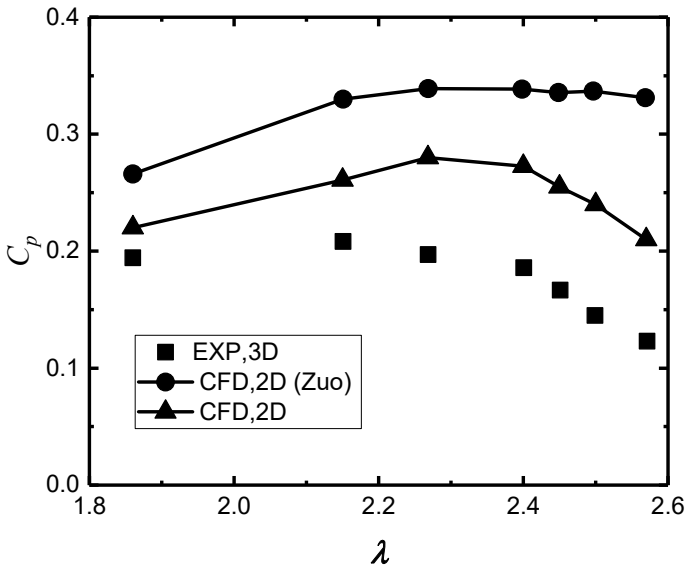

Figure 11. Comparison of experimental data and numerical simulated data for wind turbine power coefficient.

3.2. Influence of Tip Speed Ratio

Five tip speed ratios, λ = 1, 1.5, 2, 2.5, and 3, were investigated. Figure 12 shows the variation of the blade tangential force coefficient C_t with azimuth at different tip speed ratios. In a rotation cycle, the C_t basically exhibits a double-peak variation. The maximum tangential force coefficient $C_{t\,max}$ and its corresponding azimuth $\theta_{ct.max}$, with increasing tip speed ratio, increase first and then remain unchanged. It can be seen that when the blade moves to the downwind side, the C_t value is around 0 due to the influence of the upstream wakes.

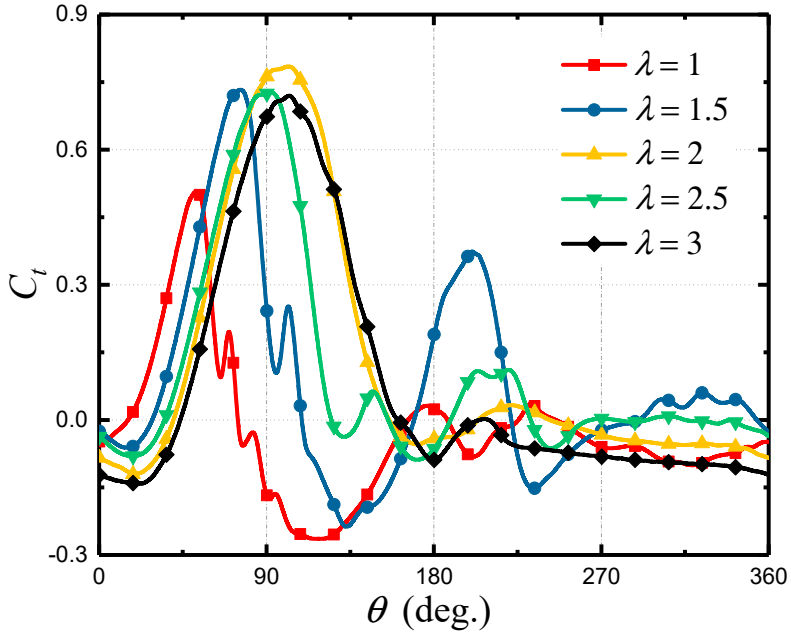

Figure 12. Tangential force coefficient of a blade with azimuth.

In [20], the VAWT consists of NACA0015 airfoil, which is a thin thickness airfoil. The dynamic stall phenomenon of this kind of wind turbine is expressed as the formation, development and shedding of the leading edge vortex on the blade or airfoil. The VAWT selected in this paper consists of the NACA0022 airfoil, which is a medium thickness airfoil. In [41], the aerodynamic performance of the four VAWT airfoils (NACA0012, NACA0022, NACA5522, and LS0421) was compared. The study found that the NACA0022 airfoil performs better at small tip speed ratios. The dynamic stall phenomenon is not exactly the same as the above literature. The main difference is that there is not only the leading edge vortex on the blade, but also a trailing edge vortex with the same direction of rotation.

Figure 13 shows the vorticity (normalized to $c\omega_z/U_\infty$) contour at specific azimuths for blade 1 during a cycle at λ = 1.5. For ease of understanding, the correspondence between vortex and C_t is indicated by arrows. It should be pointed out that only under this condition, the dynamic stall occurs twice, which is represented by two distinct peaks on the C_t curve, which is the same as the case studied in [11]. The first dynamic stall has gone through four stages a, b, c, and d. The α at point a is small, resulting in a minor C_t. As the angle of attack increases with azimuth, C_t increases significantly. The azimuth of point b corresponds to the maximum of C_t, in which the flow separation from the trailing edge almost rolls up to the leading edge. It can be considered that the movement process of the blade in range a to b is in keeping with the static stall feature. At azimuth c, a leading edge vortex appears, and the vortex adheres to the surface and keep on growing. Under the influence of the leading edge vortex and the non-slip wall condition, a secondary vortex whose rotation direction is opposite to the leading edge vortex is formed. Point d is the minimum of C_t. At this time, the leading-edge vortex extends to one chord length above the suction side, while the boundary layer rolls up and forms a trailing edge vortex close to the surface. Those two vortices interact with each other and obtain circulation in the shear layer to strengthen the vorticity. After that, the leading edge vortex and the trailing edge vortex gradually shed off, and the boundary layer reattaches to the leading edge. The first dynamic stall ends. At the same time, the second dynamic stall occurs on the downwind side. The four typical moments (e, f, g, and h) correspond to the formation, development, and shedding of the leading-edge vortex, and the reattachment of the boundary layer at leading edge. Different from the upwind-side dynamic stall, the trailing edge vortex on the downwind side is not formed on the surface, which is affected by the free flow below the rotor. In this figure, the trajectories of the leading edge vortex and the trailing edge vortex on the upwind and the downwind side can also be observed.

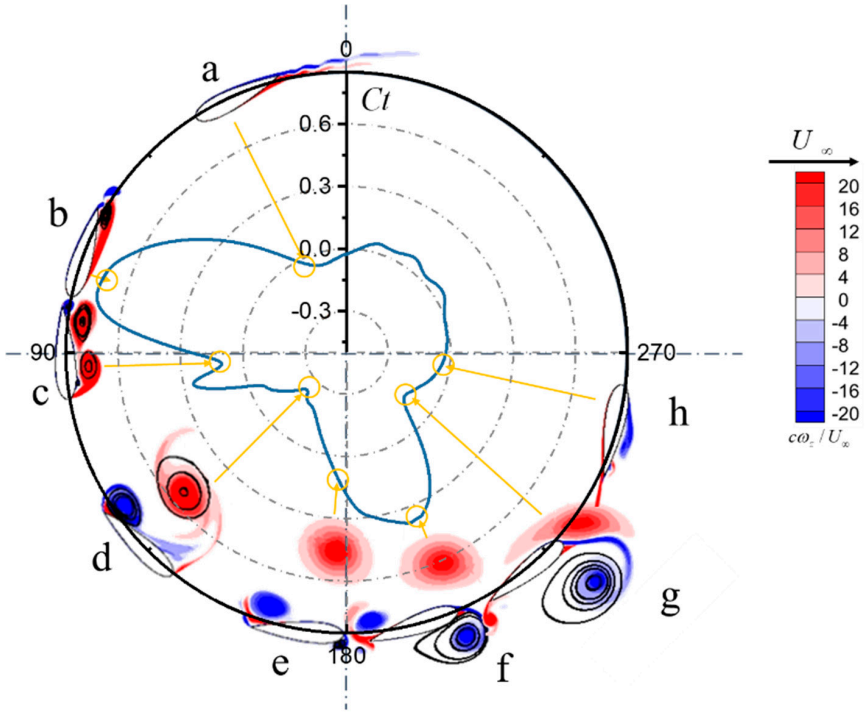

Figure 13. Tangential force coefficient of a blade and vorticity contours with λ = 1.5.

Figure 14 shows the vorticity (normalized to $c\omega_z/U_\infty$) contours of the blade 1 for selected azimuth at different tip speed ratios. The major vortex structure and its motion state can be clearly observed. The development and their interaction of the leading edge vortex and a pair of trailing edge vortices can be found out. Comparing the vorticity contours, we can see the delay effect of the VAWT dynamic stall at high tip speed ratio. The delay effect means that as the tip speed ratio rises, the VAWT dynamic stall is delayed. The higher the tip speed ratio, the smaller the amplitude of the angle of attack and the relative speed, and the less evidently the dynamic stall occurs.

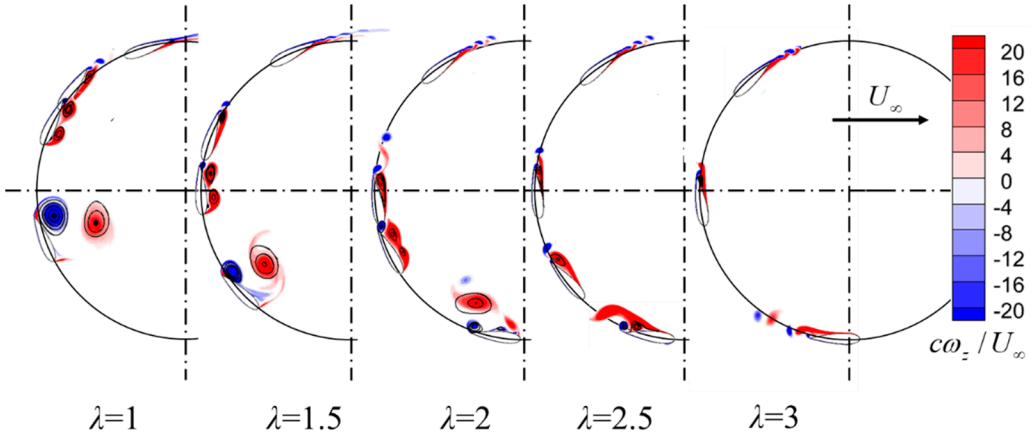

Figure 14. Vorticity contours with different λ for selected azimuth.

Figure 15 shows the vorticity contours for different tip speed ratios at θ = 120°. In order to facilitate the observation and comparison, the coordinates of the blade are transformed. Although the blades rotate to the same azimuth, the vorticity contours are totally different. It can be considered that these five vorticity fields (from λ = 3 to λ = 1) can represent the VAWT dynamic stall at different stages. At the same azimuth, the high tip speed ratio corresponds to a small angle of attack, and the dynamic stall delay is more distinct at high tip speed ratios.

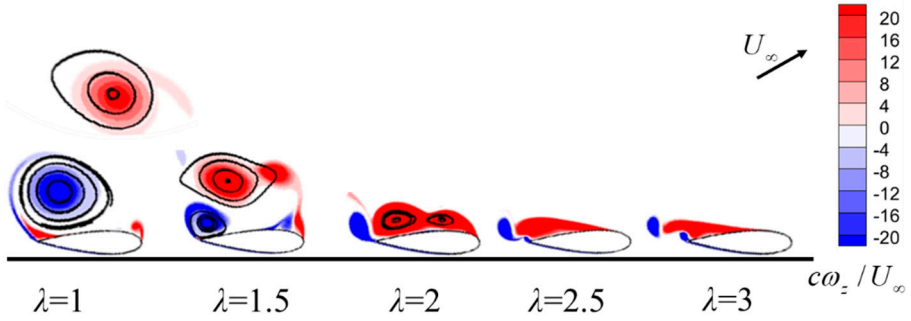

Figure 15. Vorticity contours with different λ at θ = 120°.

Figure 16 shows the azimuth of the maximum tangential force coefficient $\theta_{ct.max}$ as a function of the tip speed ratio, and the horizontal axis is divided by five tip speed ratios. It can be seen from the figure that the $\theta_{ct.max}$ increases first and at a level between 90° and 100° with the increase of λ. Figure 17 shows the angle of attack of the maximum tangential force coefficient $\alpha_{ct.max}$ as a function of the tip speed ratio. It was found that when $\lambda \leq 2$, the $\alpha_{ct.max}$ is approximately above 26°, which is similar to the result observed in [15]. As can be seen from Figure 10, the relative angle of attack of the blade can be higher than 26° only when $\lambda \leq 2$; when $\lambda > 2$, $\theta_{ct.max} = \theta_{\alpha,\,max}$, where $\theta_{\alpha,\,max}$ represents the azimuth of the maximum angle of attack, which is also observed in Figure 17. In summary, it can be considered that when the blade moves to an angle of attack higher than 26°, or when moving to the maximum angle of attack (the maximum angle of attack α_{max} is less than 26°), the tangential force reaches a maximum value and the flow begins to stall. The specific reasons have been analyzed above, as shown in Figures 10 and 15.

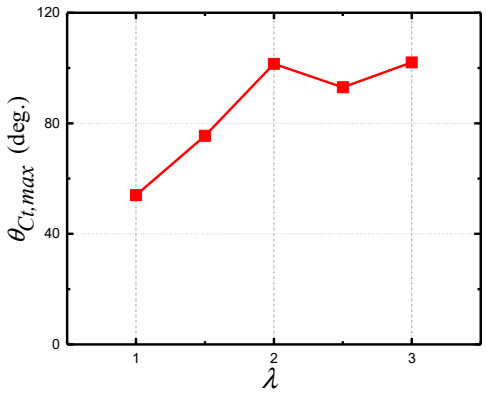

Figure 16. $\theta_{ct.max}$ of a blade with λ.

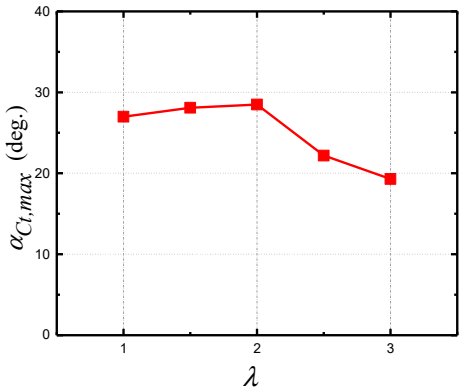

Figure 17. $\alpha_{ct.max}$ of a blade with λ.

Figures 18 and 19 show the change of the azimuth $\theta_{ct.mix}$ and the angle of attack $\alpha_{ct.mix}$ with the tip speed ratio, respectively, where the minimum tangential force coefficient is located. It was found that $\theta_{ct.mix}$ rised with the tip speed ratio, while $\alpha_{ct.mix}$ reduced with the tip speed ratio. The tangential force stall azimuth interval is defined as $\theta_{ct.stall}$,

$$\theta_{ct.stall}, = \theta_{ct.mix} - \theta_{ct.max}. \quad (8)$$

Figure 20 shows the variation of $\theta_{ct.stall}$, with the tip speed ratio.

It is found that the tangential force stall azimuth is about 60° ± 5° when the blade is moving at a low tip speed ratio (i.e., $\alpha_{max} > 26°$); while the stall azimuth is about 80° ± 5° at high tip speed ratio.

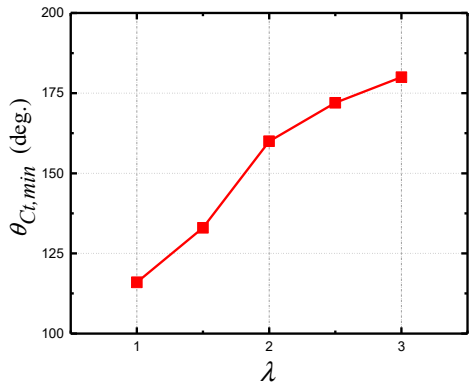

Figure 18. $\theta_{ct.mix}$ of a blade with λ.

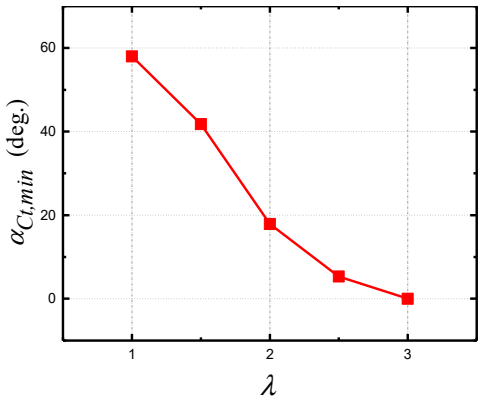

Figure 19. $\alpha_{ct.mix}$ of a blade with λ.

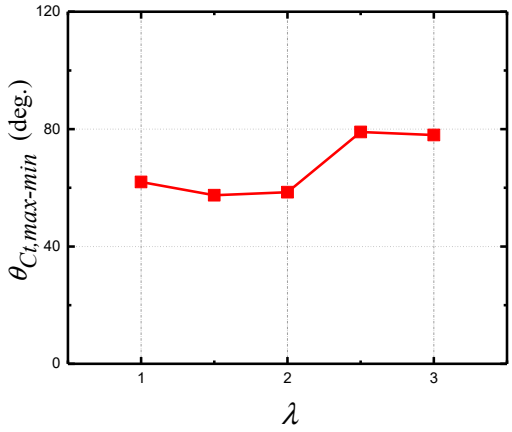

Figure 20. $\theta_{ct.max\text{-}mix}$ of a blade with λ.

3.3. Influence of Plasma Actuation Flow Control Strategy on VAWT

In this part, the wind turbine is selected to operate at a tip speed ratio of 2.15. Because according to Figure 11, when the tip speed ratio is 2.15, the wind turbine has a maximum power coefficient in the experiment.

The effect of the plasma actuator positions on VAWT was studied. The actuator is placed at 5% c, 30% c, 50% c, 70% c, and 90% c from the leading edge, respectively. C_p of the VAWT with different plasma actuation positions is shown in Table 2. The baseline case is uncontrolled VAWT rotate at a tip speed ratio of 2.15. In contrast, it has been found that using plasma actuator at these five positions can increase the C_p of the VAWT. The optimal position is at 30% c and the power is increased by 36%. Figure 21 shows the variation of the tangential force coefficient with azimuth at different plasma actuator positions. In general, the actuation increases the maximum tangential force of the blade. At $15° < \theta < 165°$, plasma actuation can significantly increase the tangential force. However, when $\theta > 165°$, the actuation has less effect.

Table 2. C_p with different plasma actuator positions.

Position of the Plasma Actuator	C_p
Baseline	0.261
5% c	0.324
30% c	0.358
50% c	0.355
70% c	0.315
90% c	0.262

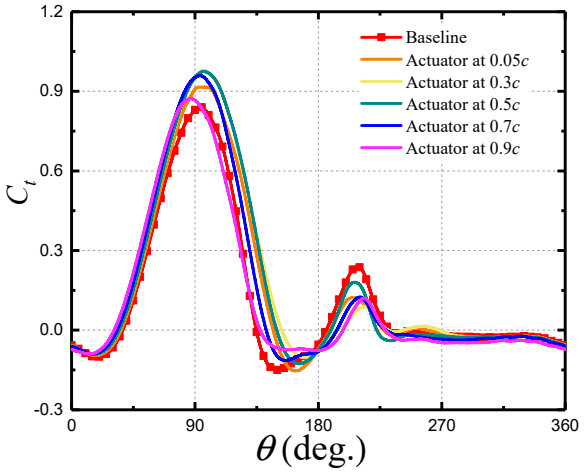

Figure 21. Tangential force coefficient with azimuth at different plasma actuator positions.

Figure 22 shows the relative velocity contour with relative velocity streamlines. The flow fields before and after the controlled (the plasma actuator is at 30% c) were compared. When the actuator is at 30% c, plasma actuation can suppress flow separation, but does not completely eliminate flow separation. The baseline case forms a secondary vortex at θ = 135°, while the controlled case is formed at θ = 155°. Therefore, arranging the plasma actuator at 30% c, plasma actuation will delay the formation of the secondary vortex. It can also be seen from the comparison that the plasma actuation can accelerate the detachment of the vortex on the blade.

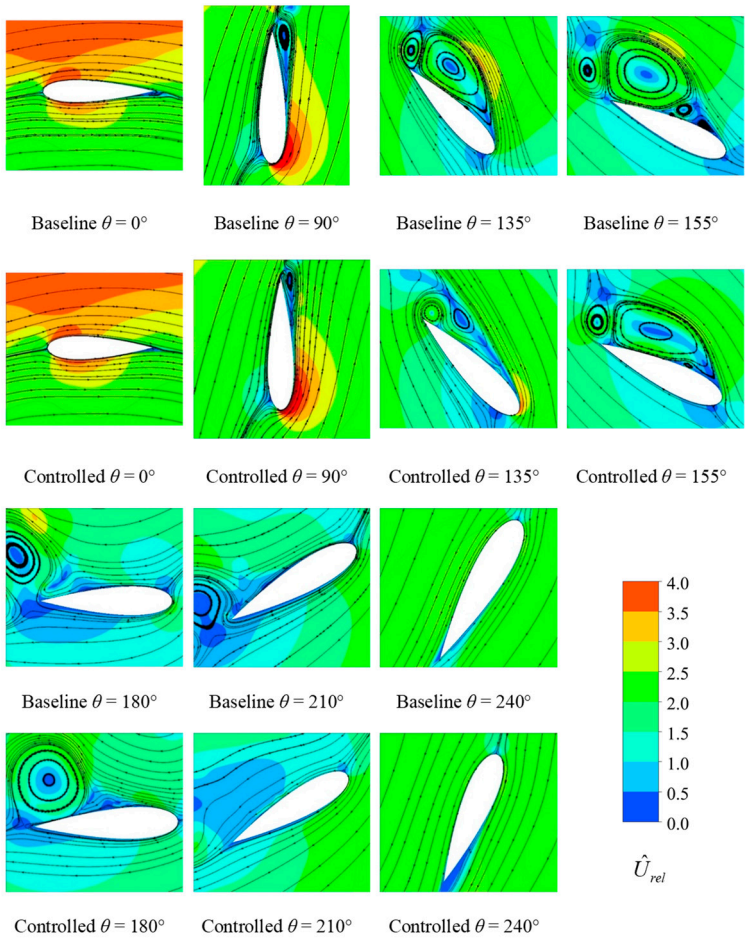

Figure 22. Relative streamlines and relative velocity contours with azimuth for baseline and plasma controlled case (actuator at 30% *c*).

Ten control strategies were studied. The research schemes are shown in Tables 1 and 3. According to that mentioned above, when the tip speed ratio is 2.15, it can be predicted that the H-type VAWT tangential force starts to stall at $\theta = 95° \pm 5°$, and ends the stall at $\theta = 155° \pm 5°$. The plasma actuation control strategies are developed accordingly.

The specific control strategy is shown in Table 3. Case 1 is a baseline and no plasma actuation is applied. In Case 2, the plasma is continuously pulsed on each of the blades during the rotation cycle. In Cases 3–10, the plasma is pulsed in different azimuthal intervals.

Table 3. Strategies of plasma actuation control.

Strategy	Actuation Azimuth Interval	Strategy	Actuation Azimuth Interval
Case 1	No control	Case 6	70° to 150°
Case 2	Global control	Case 7	60° to 150°
Case 3	90° to 160°	Case 8	60° to 130°
Case 4	90° to 150°	Case 9	60° to 120°
Case 5	80° to 150°	Case 10	50° to 110°

Figure 23 shows the variation of the tangential force coefficient with azimuth at the plasma actuation. It can be confirmed from the Case 1 curve that the above prediction is accurate. In general, within $90° < \theta < 180°$, the tangential force coefficient is significantly improved by plasma, and has little effect on other azimuths. Cases 3, 4, and 7–9 show that the end azimuth of the actuation has little impact on the tangential force. Case 4–7 are used to investigate the effect of the starting actuation

azimuth on the tangential force. It is found that the early actuation increases the tangential force and the peak value is higher. Cases 9 and 10 are a set of controlled trials. In the case of the same actuation interval size, the influence of the starting and ending position on the tangential force is studied. There is no significant difference between Case 9 and 10, however, when $\theta > 150°$ the tangential force of Case 10 is lower than Case 9.

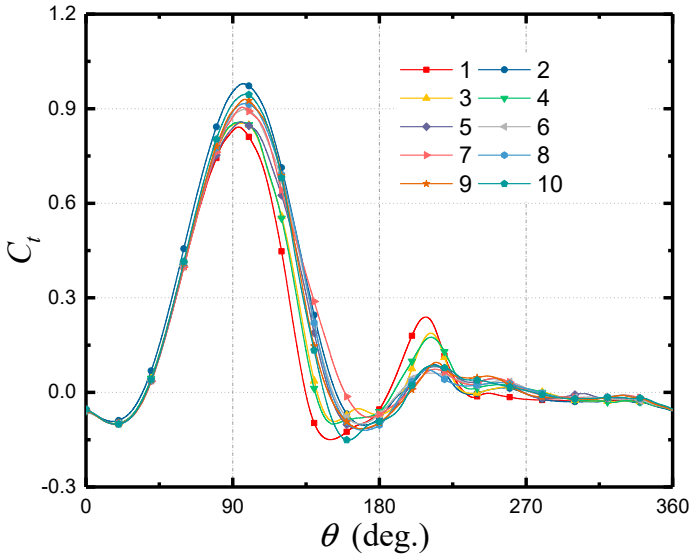

Figure 23. Tangential force coefficient of a blade with azimuth at plasma actuation.

Aerodynamic figure of merit (AFM) [42] is introduced to determine whether the active flow control strategy is cost effective. AFM is defined as

$$\text{AFM} = \frac{P_{\text{controlled}} - P_{\text{actuators}}}{P_{\text{baseline}}} \tag{9}$$

where $P_{\text{controlled}}$ is the power of controlled VAWT, $P_{\text{actuators}}$ is the plasma actuators consumption, and P_{baseline} is the power of uncontrolled VAWT. When AFM > 1, the power consumption of actuators is less than the additional output of VAWT, and the control strategy is feasible.

Table 4 shows the C_p and AFM for different control strategies. The power of VAWT can be directly calculated from the above, and the energy consumption of the plasma exciter is 6.67 W/m [16,17,43]. It can be seen that Case 2 increases the C_p up to 36%, but it is not suitable. Cases 6–10 are feasible, and the maximum C_p can be increased by 34.3%, in which Case 9 is optimal. Considering the consumption of the plasma actuator, Case 9 has the highest AFM value, which means that Case 9 consumes less energy and produces considerable power. Within the scope of the study, it is necessary to apply control in advance to achieve better control results.

Table 4. C_p and AFM at plasma actuation.

Strategy	C_p	AFM	Strategy	C_p	AFM
Case 1	0.261	-	Case 6	0.331	1.033
Case 2	0.358	0.304	Case 7	0.343	1.048
Case 3	0.296	0.928	Case 8	0.331	1.062
Case 4	0.299	0.968	Case 9	0.326	1.072
Case 5	0.310	0.982	Case 10	0.322	1.056

4. Conclusions

In this paper, the phenomenological model and URANS simulation are used to study the VAWT dynamic stall phenomenon with different tip speed ratios. The effects of plasma actuation on the aerodynamic performance of the blade are explored, and the following conclusions are drawn:

1. As the dynamic stall of the vertical-axis wind turbine occurs, the boundary layer separation moves from the trailing edge to the leading edge. The boundary layer will reattach to the blade surface with the leading edge vortex and the secondary vortex shedding. With the increase of the tip speed ratio, the delay effect of the dynamic stall is more obvious.
2. The tip speed ratio affects the maximum and minimum values of the tangential force for a blade. When the tip speed is low, the maximum tangential force is at the azimuth of the $\alpha = 26°$, and the minimum value is at the following 60° ± 5° azimuth. When the tip speed is high, the maximum tangential force is at the azimuth where the maximum angle of attack is, and the minimum is at the following 80° ± 5° azimuth.
3. The pulsed plasma actuation can effectively enhance the power of the vertical-axis wind turbine, and the actuation at 60° to 120° azimuth is optimal.

Author Contributions: Conceptualization, L.M.; Data curation, L.M.; Formal analysis, L.M.; Funding acquisition, X.W.; Investigation, L.M.; Project administration, X.W.; Supervision, J.Z.; Validation, J.Z. and S.K.; Writing—original draft, L.M.; Writing—review & editing, L.M.

Funding: This work was supported by National Natural Science Foundation of China (no. 51576065, 51876063).

Conflicts of Interest: The authors declare no conflicts of interest.

References

1. Kantrowitz, A.R. A survey of physical phenomena occurring in flight at extreme speeds. In Proceedings of the Conference on High-Speed Aeronautics, New York, NY, USA, 20–22 January 1955; Volume 1955, pp. 335–339.
2. Roth, J.R.; Sherman, D.M.; Wilkinson, S.P. *Boundary Layer Flow Control with a One Atmosphere Uniform Glow Discharge Surface Plasma*; American Institute of Aeronautics and Astronautics: Reston, VA, USA, 1998.
3. Post, M.L.; Corke, T. Separation control using plasma actuators: Dynamic stall vortex control on oscillating airfoil. *AIAA J.* **2006**, *44*, 3125–3135. [CrossRef]
4. Liu, Y.; Kolbakir, C.; Hu, H.; Meng, X.; Hu, H. An experimental study on the thermal effects of duty-cycled plasma actuation pertinent to aircraft icing mitigation. *Int. J. Heat Mass Transf.* **2019**, *136*, 864–876. [CrossRef]
5. McCroskey, W. *The Phenomenon of Dynamic Stall*; NASA TM-81264; National Aeronuatics and Space Administration Moffett Field Ca Ames Research Center: Mountain View, CA, USA, 1981.
6. Araya, D.B.; Dabiri, J.O. Vertical axis wind turbine in a falling soap film. *Phys. Fluids* **2015**, *27*, 091108. [CrossRef]
7. Liu, Q.; Miao, W.; Li, C. Effects of trailing-edge movable flap on aerodynamic performance and noise characteristics of VAWT. *Energy* **2019**, *192*, 58–79.
8. Liu, Q.; Hao, W.; Li, C.; Miao, W.; Ding, Q. Numerical Simulation on the Forced Oscillation of Rigid Riser with Helical Strakes in Different Section Shapes. *Ocean Eng.* **2019**, *191*, 106439. [CrossRef]
9. Zhu, H.; Hao, W.; Li, C. Numerical investigation on the effects of different wind directions, solidity, airfoils and building configurations on the aerodynamic performance of building augmented vertical axis wind turbines. *Int. J. Green Energy* **2019**, *16*, 1216–1230.
10. Miao, W.; Li, C.; Wang, Y.; Xiang, B.; Liu, Q.; Deng, Y. Study of Adaptive Blades in Extreme Environment using Fluid-Structure Interaction Method. *J. Fluids Struct.* **2019**, *91*, 102734. [CrossRef]
11. Zhu, C.; Wang, T. Comparative Study of Dynamic Stall under Pitch Oscillation and Oscillating Freestream on Wind Turbine Airfoil and Blade. *Appl. Sci.* **2018**, *8*, 1242. [CrossRef]
12. Yanzhao, Y.; Guo, Z.; Zhang, Y.; Jinyama, H.; Li, Q. Numerical Investigation of the Tip Vortex of a Straight-Bladed Vertical Axis Wind Turbine with Double-Blades. *Energies* **2017**, *10*, 1721.

13. Qian, C.; Liu, X.; Ji, H.S.; Kim, K.C.; Yang, B. Aerodynamic Analysis of a Helical Vertical Axis Wind Turbine. *Energies* **2017**, *10*, 575.
14. Sato, S.; Yokoyama, H.; Iida, A. Control of Flow around an Oscillating Plate for Lift Enhancement by Plasma Actuators. *Appl. Sci.* **2019**, *9*, 776. [CrossRef]
15. Phan, M.K.; Shin, J. Numerical investigation of aerodynamic flow actuation produced by surface plasma actuator on 2D oscillating airfoil. *Chin. J. Aeronaut.* **2016**, *29*, 882–892. [CrossRef]
16. Greenblatt, D.; Lautman, R. Inboard/outboard plasma actuation on a vertical-axis wind turbine. *Renew. Energy* **2015**, *83*, 1147–1156. [CrossRef]
17. Benharav, A.; Greenblatt, D. Plasma-based feed-forward dynamic stall control on a vertical axis wind turbine. *Wind Energy* **2016**, *19*, 3–16. [CrossRef]
18. Fujisawa, N.; Shibuya, S. Observations of dynamic stall on Darrieus wind turbine blades. *J. Wind Eng. Ind. Aerodyn.* **2001**, *89*, 201–214. [CrossRef]
19. Wang, X.D.; Ye, Z.; Kang, S.; Hu, H. Investigations on unsteady aerodynamic characteristics of a horizontal-axis wind turbine during dynamic yaw process. *Energies* **2019**, *12*, 3124. [CrossRef]
20. Buchner, A.J.; Soria, J.; Honnery, D.; Smits, A.J. Dynamic stall in vertical axis wind turbines: Scaling and topological considerations. *J. Fluid Mech.* **2018**, *841*, 746–766. [CrossRef]
21. Christian, M.; Christophe, L.; Ion, P. Appropriate Dynamic-Stall Models for Performance Predictions of VAWTs with NLF Blades. *Int. J. Rotating Mach.* **1998**, *4*, 129–139.
22. Zuo, W.; Wang, X.; Kang, S. Numerical simulations on the wake effect of H-type vertical axis wind turbines. *Energy* **2016**, *106*, 691–700. [CrossRef]
23. Buchner, A.J.; Soria, J.; Honnery, D.; Smits, A.J. Dynamic stall in vertical axis wind turbines: Comparing experiments and computations. *J. Wind Eng. Ind. Aerodyn.* **2015**, *146*, 163–171. [CrossRef]
24. Shyy, W.; Jayaraman, B.; Andersson, A. Modeling of glow discharge-induced fluid dynamics. *J. Appl. Phys.* **2002**, *92*, 6434–6443. [CrossRef]
25. Massines, F.; Rabehi, A.; Decomps, P.; Ben Gadri, R.; Ségur, P.; Mayoux, C. Experimental and theoretical study of a glow discharge at atmospheric pressure controlled by dielectric barrier. *J. Appl. Phys.* **1998**, *83*, 2950–2957. [CrossRef]
26. Suzen, Y.B.; Huang, G.; Jacob, J.; Ashpis, D. Numerical simulations of plasma based flow control applications. *AIAA Pap.* **2005**, *4633*, 2005.
27. Abdollahzadeh, M.; Páscoa, J.; Oliveira, P.J.; Abdollahzadehsangroudi, M.; Páscoa, J. Modified split-potential model for modeling the effect of DBD plasma actuators in high altitude flow control. *Curr. Appl. Phys.* **2014**, *14*, 1160–1170. [CrossRef]
28. Abdollahzadeh, M.; Pascoa, J.; Oliveira, P.J.; Abdollahzadehsangroudi, M.; Páscoa, J. Implementation of the classical plasma-fluid model for simulation of dielectric barrier discharge (DBD) actuators in OpenFOAM. *Comput. Fluids* **2016**, *128*, 77–90. [CrossRef]
29. Abdollahzadeh, M.; Pascoa, J.C.; Oliveira, P.J. Comparison of DBD plasma actuators flow control authority in different modes of actuation. *Aerosp. Sci. Technol.* **2018**, *78*, 183–196. [CrossRef]
30. Ma, L.; Wang, X.; Zhu, J.; Kang, S. Effect of DBD plasma actuation characteristics on turbulent separation over a hump model. *Plasma Sci. Technol.* **2018**, *20*, 139–149. [CrossRef]
31. Ebrahimi, A.; Hajipour, M. Flow separation control over an airfoil using dual actuation of DBD plasma actuators. *Aerosp. Sci. Technol.* **2018**, *79*, 658–668. [CrossRef]
32. Howell, R.; Qin, N.; Edwards, J.; Durrani, N. Wind tunnel and numerical study of a small vertical axis wind turbine. *Renew. Energy* **2010**, *35*, 412–422. [CrossRef]
33. Maden, I.; Maduta, R.; Kriegseis, J.; Jakirlić, S.; Schwarz, C.; Grundmann, S.; Tropea, C. Experimental and computational study of the flow induced by a plasma actuator. *Int. J. Heat Fluid Flow* **2013**, *41*, 80–89. [CrossRef]
34. Jayaraman, B.; Thakur, S.; Shyy, W. Modeling of fluid dynamics and heat transfer induced by dielectric barrier plasma actuator. *J. Heat Transf.-Trans. ASME* **2007**, *129*, 517–525. [CrossRef]
35. Jayaraman, B.; Shyy, W. Modeling of dielectric barrier discharge-induced fluid dynamics and heat transfer. *Prog. Aerosp. Sci.* **2008**, *44*, 139–191. [CrossRef]
36. Ostos, I.; Ruiz, I.; Gajic, M.; Gómez, W.; Bonilla, A.; Collazos, C. A modified novel blade configuration proposal for a more efficient VAWT using CFD tools. *Energy Convers. Manag.* **2019**, *180*, 733–746. [CrossRef]

37. Bai, H.; Chan, C.; Zhu, X.; Li, K. A numerical study on the performance of a Savonius-type vertical-axis wind turbine in a confined long channel. *Renew. Energy* **2019**, *139*, 102–109. [CrossRef]
38. Sagharichi, A.; Zamani, M.; Ghasemi, A. Effect of solidity on the performance of variable-pitch vertical axis wind turbine. *Energy* **2018**, *161*, 753–775. [CrossRef]
39. Wong, K.H.; Chong, W.T.; Poh, S.C.; Shiah, Y.-C.; Sukiman, N.L.; Wang, C.-T. 3D CFD simulation and parametric study of a flat plate deflector for vertical axis wind turbine. *Renew. Energy* **2018**, *129*, 32–55. [CrossRef]
40. Qin, N.; Howell, R.; Durrani, N.; Hamada, K.; Smith, T. Unsteady flow simulation and dynamic stall behaviour of vertical axis wind turbine blades. *Wind Eng.* **2011**, *35*, 511–527. [CrossRef]
41. Danao, L.A.; Qin, N.; Howell, R. A numerical study of blade thickness and camber effects on vertical axis wind turbines. *Proc. Inst. Mech. Eng. Part A* **2012**, *226*, 867–881. [CrossRef]
42. Stalnov, O.; Kribus, A.; Seifert, A. Evaluation of active flow control applied to wind turbine blade section. *J. Renew. Sustain. Energy* **2010**, *2*, 063101. [CrossRef]
43. Corke, T.; Post, M.L.; Orlov, D.M. Single-dielectric barrier discharge plasma enhanced aerodynamics: Concepts, optimization, and applications. *J. Propuls. Power* **2008**, *24*, 935–945. [CrossRef]